이학석사 학위논문

Recalibrating Black Hole Mass Estimators Using High S/N Ratio Keck Spectra

KECK 스펙트럼을 이용한 블랙 홀 질량 측정법 보정

2012년 6월

서울대학교 대학원

물리·천문학부 천문학 전공

박 다 우

Recalibrating Black Hole Mass Estimators Using High S/N Ratio Keck Spectra

A thesis submitted in partial fulfillment of the final requirement for the degree of

Master of Science

Astronomy Program

Department of Physics and Astronomy

Seoul National University

Candidate: **Dawoo Park**

Supervisor: **Jong-Hak Woo**

June 2012

Abstract

We compare and recalibrate black hole mass estimators using a sample of 36 moderate-luminosity Type 1 AGNs selected at $z \sim 0.4$. Combining the high S/N ratio Keck spectra with SDSS archival spectra, we perform a detailed multi-component spectral decomposition analysis and measure the width and luminosity of the Mg II 2798Å, Hβ 4861Å and Hα 6563Å lines, to calibrate single-epoch mass estimators. By using the best-calibrated Hβ line width and AGN continuum luminosity at 5100Å as reference values, we derive black hole mass ($\mathrm{M_{BH}}$) recipes based on various combinations of the line widths and luminosities. After applying new calibrations, mass estimators based on the combination of line dispersion and luminosity show best agreement within 0.16 dex scatter while mass estimators based on the FWHM and luminosity of emission lines are also reliable within 0.27 dex.

Keywords: black hole physics — galaxies: active — galaxies: evolution — quasars: general

Student Number: 2010 − 20389

Contents

Chapter 1

Introduction

It is generally believed that the growth of supermassive black holes (BHs) is closely related with galaxy evolution as implied by the relatively tight correlations between BH mass (M_{BH}) and galaxy properties, e.g., the M_{BH}-stellar velocity dispersion relation in the present-day universe (Ferrarese & Merritt 2000; Gebhardt et al. 2000; Gültekin et al. 2009; Woo et al. 2010). For determining M_{BH} as one of the most fundamental parameters in investigating the nature of BH-galaxy coevolution, various methods have been devised.

For broad-line (Type 1) AGNs, M_{BH} can be determined from the kinematics of broad-line region (BLR), which are generally believed to be virialized by the gravitational potential of the central BH (see Peterson 1993, Park et al. 2012). By combining the measured gas velocity from the width of broad emission lines and the measured photon-travel time to BLR as the size of BLR using the reverberation mapping technique, M_{BH} has been determined for ~ 50 local Seyfert 1 galaxies and QSOs based on the virial assumption (e.g., Kaspi et al. 2000; Perterson et al. 2004; Bentz et al. 2009; Denney et al. 2010; Barth et al. 2011; Grier et al. 2012).

A more popularly-used indirect method is the so-called single-epoch (SE) method, which is applicable to a large sample of AGNs based on single spectroscopic observations. Instead of direct reverberation-mapping, this method relies on the empirical relation between the BLR size and AGN continuum luminosity, enabling M_{BH} estimation using single-epoch spectra (e.g., Wandel et al. 1999; Kaspi et al. 2000, 2005; Bentz et al. 2009). Although the uncertainties of M_{BH} estimates from the SE method is much larger than direct reverberation measurements (see discussion by Park et al. 2012), the SE method can be applied to statistical studies of AGN M_{BH}(e.g., Woo & Urry 2002; Salviander et al. 2007; Treu et al. 2007 ; Bennert et al. 2011; Shen et al. 2011).

Although the SE method has been best-calibrated for Hβ and Hα lines since the most reverberation mapping results have provided the Hβ or Hα BLR size, various other broad-emission lines can be also used for estimating M_{BH}, including rest-frame UV lines (C IV and Mg II ; Vestergaard & Peterson 2006 , Wang et al. 2009 , Shen & Liu 2012), and near-IR lines (Pα ; Kim et al. 2010). For AGNs at $z > 0.6$, the Balmer lines are redshifted out of optical spectral range, hence the rest-frame UV lines can substitute the Balmer lines. The Mg II 2798Å line is a prominent line for AGNs at $0.6 < z < 2$ (e.g., McLure & Dunlop 2004; Woo 2008; McGill et al. 2008) while the C IV 1549Å line can be used for higher-z AGNs (e.g., Vestergaard et al. 2004; Vestergaard et al. 2006; Assef et al. 2011; Shen & Liu 2012).

Although direct reverberation mapping results based on Mg II have not been reported due to the lack of line flux variability (Woo 2008), a Mg II-based SE estimator has been devised by calibrating AGN continuum luminosity at 3000Å with the Hβ-emitting BLR size, and by comparing widths of Mg II and Hβ (McLure & Dunlop 2002; McLure & Dunlop 2004). Consequently, the uncertainties of M_{BH} based on Mg II are larger than those of Balmer lines (see McGill et al. 2008, Wang et al. 2009; Shen et al. 2011).

Another source of systematic uncertainty of Mg II-based M_{BH} comes from the complexity of the Mg II region, which is often called small blue bump (Wills et al. 1985) and presents strong Fe II features. Thus, it is necessary to subtract the Fe II for measuring the width of Mg II. Since the measured line width of Mg II can be heavily affected by Fe II subtraction, it is controversial how the underline Fe II can be best removed (Bruhweiler & Verner 2008, Tsuzuki et al. 2006, Vestergaard & Wilkes 2001). For example, Vestergaard & Wilkes (2001) provided a Fe II template directly obtained from the observed spectrum of the narrow line Seyfert 1 galaxy, I Zw 1, while Tsuzuki et al. (2006) developed a new template by adding the FeII emission under the Mg II line based on photoionization model, CLOUDY (Ferland et al. 1998). Consequently, there can be large difference of Mg II line width depending on the choice of Fe II template, leading to systematic difference between Hβ and Mg II line widths as reported by Wang et al. (2009).

Regarding gas velocity, Peterson et al. (2004) suggested that line dispersion (second moment, $\sigma_{\rm line}$) of the line profile is a better velocity indicator than full width at half-maximum (FWHM) since $\sigma_{\rm line}$ presents the virial relationship better than FWHM. FWHM measurements can be easily affected by the narrow component while line dispersions are not. In contrast, if the spectra quality is moderate as in the case of the Sloan Digital Sky Survey (SDSS) data, then the noise on the continuum can easily affect the fitting process, and wings of the line can be under/overestimated. Also, careful multi-component fitting is required for blended lines, particularly for high-mass AGNs with large line widths.

Several previous studies have calibrated various SE estimators (e.g., McLure & Jarvis 2002; Vestergaard & Peterson 2006; Wang et al. 2009; Assef et al. 2011; Shen et al. 2011; Shen & Liu 2012). However, these works were based on relatively low quality spectra and mainly used the FWHM measurements for deriving SE mass estimators. Hence, detailed calibrations using line dispersion measurements based on high quality spectra are necessary to improve the SE mass estimators, and constrain the additional uncertainties introduced to other broad line estimators.

As a pilot study, McGill et al. (2008) have used high S/N Keck spectra to calibrate mass estimators using 19 moderate-luminosity Type 1 AGNs, and presented SE mass estimators. By enlarging the sample size and dynamical range, we present the detailed comparison of Hβ, Hα, and Mg II mass estimators in this paper by combining our new data with previous spectra from McGill et al. (2008). In particular, we used more sophisticated fitting procedure including stellar population models for removing stellar lines and new FeII templates for Mg II region. We describe the sample selection, observations, and data reduction in §2, and present emission line fitting analysis and measurements in §3. Comparison between various line widths and luminosities are presented in §4, followed by the new calibrations in §5. Finally, we conclude and summarize in §6. Following cosmological parameters are used throughout the paper : $H_0 = 70$ km s^{-1} Mpc^{-1}, $\Omega_{\rm m} = 0.30$, and $\Omega_\Lambda = 0.70$.

Chapter 2

Observations & Data Reduction

2.1 Sample Selection

The sample was initially selected for measuring stellar velocity dispersions of AGN host galaxies to study the $M_{\rm BH} - \sigma_*$ relation (e.g., Treu et al. 2004; Woo et al. 2006). Readers are referred to the papers by Woo et al. (2006) and Bennert et al. (2010) for the detailed procedure of sample selection. We initially selected broad-line AGNs at $0.35 < z < 0.37$ with Hβ equivalent width and Gaussian width > 5 Å from the SDSS Data Release 2 (Woo et al. 2006; McGill et al. 2008). Then, we added additional sample by limiting $M_{\rm BH}$ smaller than 10^8 $M_\odot$ to increase the dynamical range from SDSS DR7 (Bennert et al. 2010; J.-H. Woo et al. 2012 in preparation). These targets were mostly moderate-luminosity AGN, for which AGN-to-galaxy flux ratio was relatively lower, hence stellar velocity dispersions were easier to measure. The choice of redshift was made in order to prevent two major stellar absorption features, Mg b triplet (~ 5175 Å) and Fe (5270 Å), from overlapping with sky emission lines. Calibrations of SE mass estimators were studied by McGill et al. (2008) based on the initial sample of 19 AGNs. Here, we present the enlarged sample by adding 18 lower $M_{\rm BH}$ AGNs (see Bennert et al. 2010). Table 2.2 presents the properties of all targets in the enlarged sample.

Table 2.1: Target Properties

Name (1)	z (2)	R.A. (J2000.0) (3)	Decl. (J2000.0) (4)	i' (5)	Exposure (s) (6)	S/N (blue) (7)	S/N (red) (8)	Run (9)
S01....................	0.3593	15 39 16.24	+03 23 22.07	18.89	10400	208	72	1, 4
S02....................	0.3545	16 11 11.66	+51 31 31.16	19.00	3000	71	45	1
S03....................	0.3582	17 32 03.08	+61 17 51.89	18.30	5500	239	91	1, 7
S04....................	0.3579	21 02 11.50	−06 46 45.01	18.57	2400	90	46	1
S05....................	0.3530	21 04 51.83	−07 12 09.41	18.54	12600	330	119	1, 4
S06....................	0.3684	21 20 34.18	−06 41 22.24	18.84	3300	182	31	1
S07....................	0.3517	23 09 46.14	+00 00 48.87	18.18	7200	221	105	1, 4
S08....................	0.3585	23 59 53.44	−09 36 55.63	18.49	2400	101	54	1
S09....................	0.3542	00 59 16.10	+15 38 16.10	18.38	1800	110	39	1
S10....................	0.3505	01 01 12.06	−09 45 00.81	17.97	3300	235	96	1, 6
S11....................	0.3558	01 07 15.97	−08 34 29.37	18.47	10200	238	115	1, 4
S12....................	0.3574	02 13 40.59	+13 47 56.05	18.37	1800	134	40	1
S16....................	0.3702	11 19 37.59	+00 56 20.36	19.10	600	6	6	8
S21....................	0.3532	11 05 56.18	+03 12 43.15	17.31	1500	72	74	2
S23....................	0.3511	14 00 16.65	−01 08 22.16	18.16	1800	76	106	2, 4
S24....................	0.3616	14 00 34.70	+00 47 33.43	18.29	9600	184	103	2, 4
S26....................	0.3691	15 29 22.26	+59 28 54.54	18.92	3600	123	50	2
S27....................	0.3667	15 36 51.27	+54 14 42.63	18.86	7200	179	43	2

Col. (1) : Target ID. Col. (2) : redshift from SDSS DR7. Col. (3) : Right ascension. Col. (4) : Declination. Col. (5) : Extinction-corrected i' AB magnitude from SDSS DR7 photometry. Col. (6) : Total exposure time for target. Col. (7) : Signal to noise ratio of blue part CCD, measured at rest frame wavelength 2950∼3050 Å . Col. (8) : Signal to noise ratio of red part CCD, measured at rest frame wavelength 5050∼5150 Å . Col. (9) : Observing run of each target. See Table 2.3.

Table 2.2: Target Properties

Name (1)	z (2)	R.A. (J2000.0) (3)	Decl. (J2000.0) (4)	i' (5)	Exposure (s) (6)	S/N (blue) (7)	S/N (red) (8)	Run (9)
S28..................	0.3679	16 11 56.29	+45 16 10.91	18.63	5760	152	74	3, 4
S29..................	0.3575	21 58 41.92	−01 15 00.32	18.95	3600	69	56	3
S31..................	0.3505	10 15 27.26	+62 59 11.52	18.15	9000	249	78	8, 9
SS1..................	0.3566	08 04 27.98	+52 23 06.21	18.55	9000	235	26	5
SS2..................	0.3672	09 34 55.60	+05 14 09.15	18.82	7200	122	32	5
SS4..................	0.3630	09 58 50.15	+40 03 42.33	18.74	5400	175	65	8
SS5..................	0.3733	10 07 06.25	+08 42 28.41	18.69	3600	97	46	8
SS6..................	0.3584	10 21 03.57	+30 47 55.87	18.92	5400	127	49	8
SS7..................	0.3618	10 43 31.50	−01 07 32.88	18.82	5400	161	56	8
SS8..................	0.3656	10 46 10.60	+03 50 31.26	18.45	9900	359	85	8, 9, 10
SS9..................	0.3701	12 58 38.71	+45 55 15.55	18.56	5400	178	70	8
SS10.................	0.3658	13 34 14.84	+11 42 21.52	17.83	3600	333	85	9
SS11.................	0.3732	13 52 26.90	+39 24 26.84	18.39	2400	178	48	9
SS12.................	0.3625	15 01 16.82	+53 31 02.13	17.80	5500	176	119	6
SS13.................	0.3745	15 05 41.78	+49 35 19.99	18.73	11100	202	107	7, 8
SS14.................	0.3706	21 15 31.68	−07 26 27.50	19.24	9000	168	51	6
SS15.................	0.3595	01 44 12.77	−00 06 10.54	19.46	8700	78	49	6
SS17.................	0.3554	21 44 10.62	−01 01 13.42	18.47	5400	286	63	6
SS18.................	0.3582	23 40 50.52	+01 06 35.47	18.50	7200	253	65	6

Table 2.1 continued

2.2 Observations

We observed the targets using the Keck telescope between 2003 September and 2009 April as listed in Table 2.3. We used the Low-Resolution Imaging Spectrometer (LRIS) to obtain wide spectral ranges containing broad-emission lines, Mg II (2798Å) and Hβ (4861Å) in the blue and red CCDs simultaneously. All blue spectra were taken with the 600 lines mm^{-1} grism at a pixel scale of 0.63Å×0.135" and a velocity resolution (line dispersion) of ~145 km s^{-1}, while the spectra at red CCD were obtained with the 900 lines mm^{-1} grating at a pixel scale of 0.85Å×0.215" and a resolution of ~55 km s^{-1}. Six targets were observed with the 831 lines mm^{-1} grating in the red. Exposure times for each target and their S/N are listed in Table 2.2.

Table 2.3: Journal of Observations

Run	Date	Grating (lines mm^{-1})	Slit Width (arcsec)	Seeing (arcsec)	Conditions
(1)	(2)	(3)	(4)	(5)	(6)
1	2003 Sep 3	900	1.5	~ 1	Cirrus
2	2004 May 14	900	1	~ 1	Cirrus
3	2004 May 22	831	1	~ 0.8	Clear
4	2005 Jul 7, 8	900/831	1	$\sim 0.7 - 0.9$	Clear
5	2007 Jan 24	900	1	~ 1	Clear
6	2007 Aug 18,19	831/900	1	$\sim 1 - 1.7$	Clear
7	2008 Aug 2,3	900	1	~ 0.8	Clear
8	2009 Jan 21,22	900	1	$\sim 1.1 - 1.5$	Clear
9	2009 Apr 2	900	1	~ 1.2	Cirrus
10	2009 Apr 16	900	1	~ 0.8	Clear

2.3 Data Reduction

Spectroscopic data reductions were performed using the IRAF[1] scripts developed for long-slit spectroscopic data reductions. The detailed data reductions for the red and blue were described in Woo et al. (2006) and McGill et al. (2008), respectively. Here, we briefly summarize the procedure. After a bias subtraction, cosmic rays were removed from each individual exposure using the Laplacian cosmic-ray identification software (van Dokkum 2001). Flat-fielding was performed by using internal flat images, which were taken at the location of each target. One-dimensional spectra were extracted using a 10 pixel wide aperture window, corresponding to $\sim$5 kpc for the redshift of the targets. For blue spectra, wavelength calibration was performed using Hg, Ne, Cd arc lamp images taken in the afternoon while for red spectra, sky emission lines were used for wavelength calibration. Flux calibration was performed using spectroscopic standard stars and A0V stars. A0V stars were used for red part of our spectra, and standard star named Feige 34 was used for blue part because insufficient flux in short wavelength of A0V star caused a difficulty. A0V stars were also used for sky absorption (A-band and B-band) corrections.

After the spectroscopic flux calibration, we rescaled the flux level of the 1-dimensional spectra of each target to that of SDSS g' band and r' band photometry to compensate slit losses and other uncertainties. Finally, the Galactic extinction was corrected based on the method given in Schlegel et al. (1998). Figure 2.1 and 2.2 present the reduced Keck spectra of our sample overplotted with SDSS spectra. For the spectral region of the Hα line, only SDSS spectra were presented. Note that S16 was removed from the following analyses because of the lack of the Mg II line, presumably due to high internal extinction.

[1]IRAF is distributed by the National Optical Astronomy Observatories, which are operated by the Association of Universities for Research in Astronomy, Inc., under cooperative agreement with the National Science Foundation (NSF).

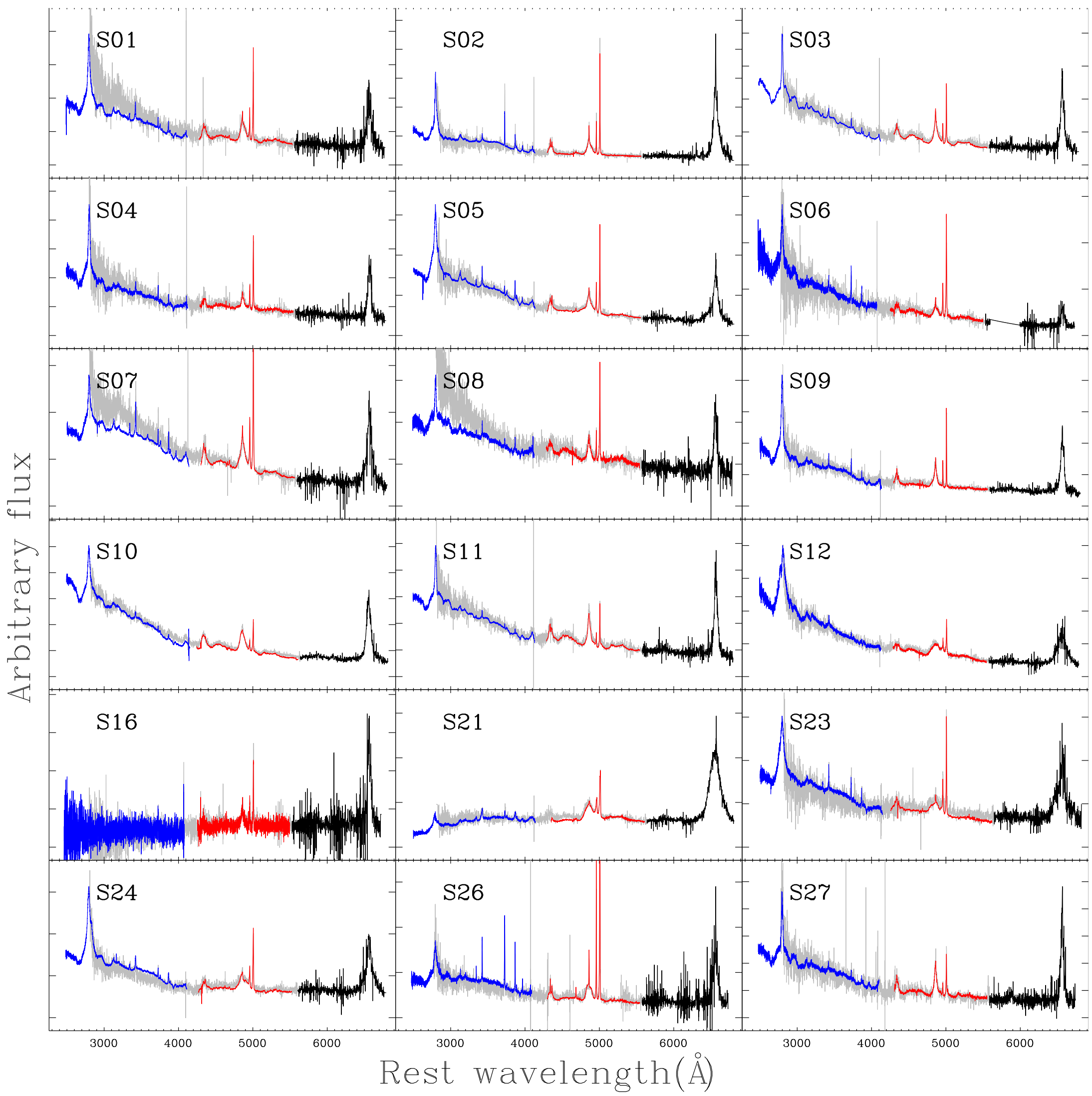

Figure 2.1: The rest-frame spectra of our sample. Blue and red spectra are taken by Keck LRIS, while grey and black data are from SDSS. All three spectra in each panel were calibrated their flux scale based on SDSS photometry, and extinction correction was also performed.

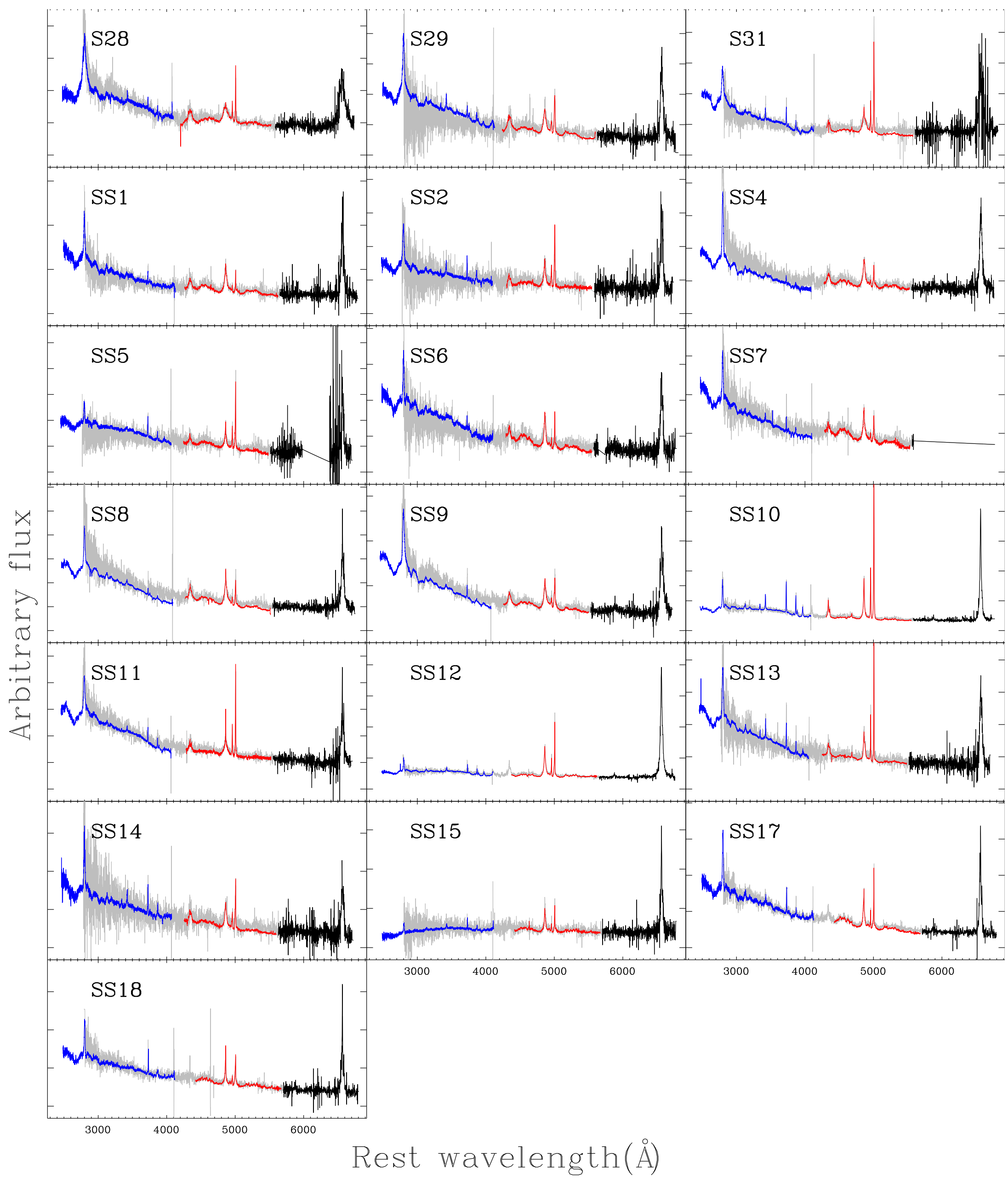

Figure 2.2: *Continued*

Chapter 3

Measurements

M_{BH} can be determined from a single spectroscopic observation by the following equation,

$$\log M_{\mathrm{BH}} = \alpha + \beta \log v + \gamma \log L, \tag{3.1}$$

where v is the line width and L is the luminosity of continuum or line and coefficients α, β, and γ can be empirically determined. To measure the line widths and luminosities, first we applied multi-component decomposition analysis to subtract various components underlying the broad line such as AGN power-law continuum, Fe II emission blends, and narrow lines. After the subtraction was performed, we measured line dispersion and FWHM as BLR velocity estimators and continuum and line luminosity as BLR size estimators. Full spectral models for the Hα, Hβ, and Mg II line regions are shown in Figure 3.1 - 3.6. The measured line and continuum properties are listed in Table 3.2. Note that Hα line properties of SS5 are omitted due to the poor fitting quality.

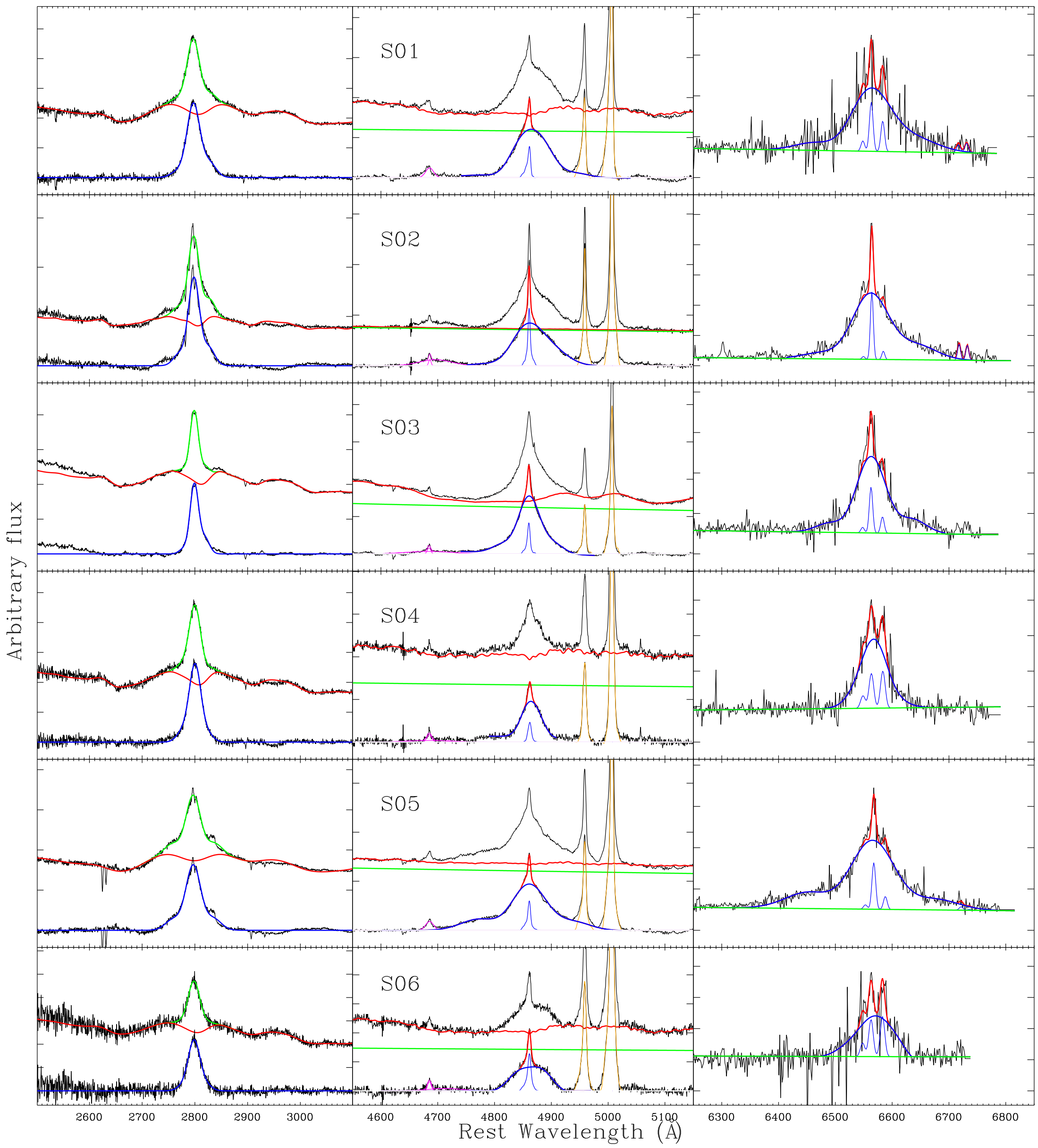

Figure 3.1: Spectral decomposition fits. *Left panel*: rest-frame spectra from LRIS blue ccd (black), pseudocontinuum of combined AGN power-law continuum and Fe II model (red), model of Mg II broad emission lines (blue). *Center panel* : rest-frame spectra from LRIS red ccd (black), pseudocontinuum of combined power-law continuum and Fe II model and stellar spectra model (red), He II broad and narrow component (magenta), O III narrow component (orange), Hβ narrow component (blue, thin), Hβ broad component (blue, thick). *Right panel* : near the Hα region of rest-frame spectra from SDSS DR7 (black), AGN power-law continuum (green), total Hα model (red), Hα and N II narrow component (blue, thin), Hα broad component (blue, thick).

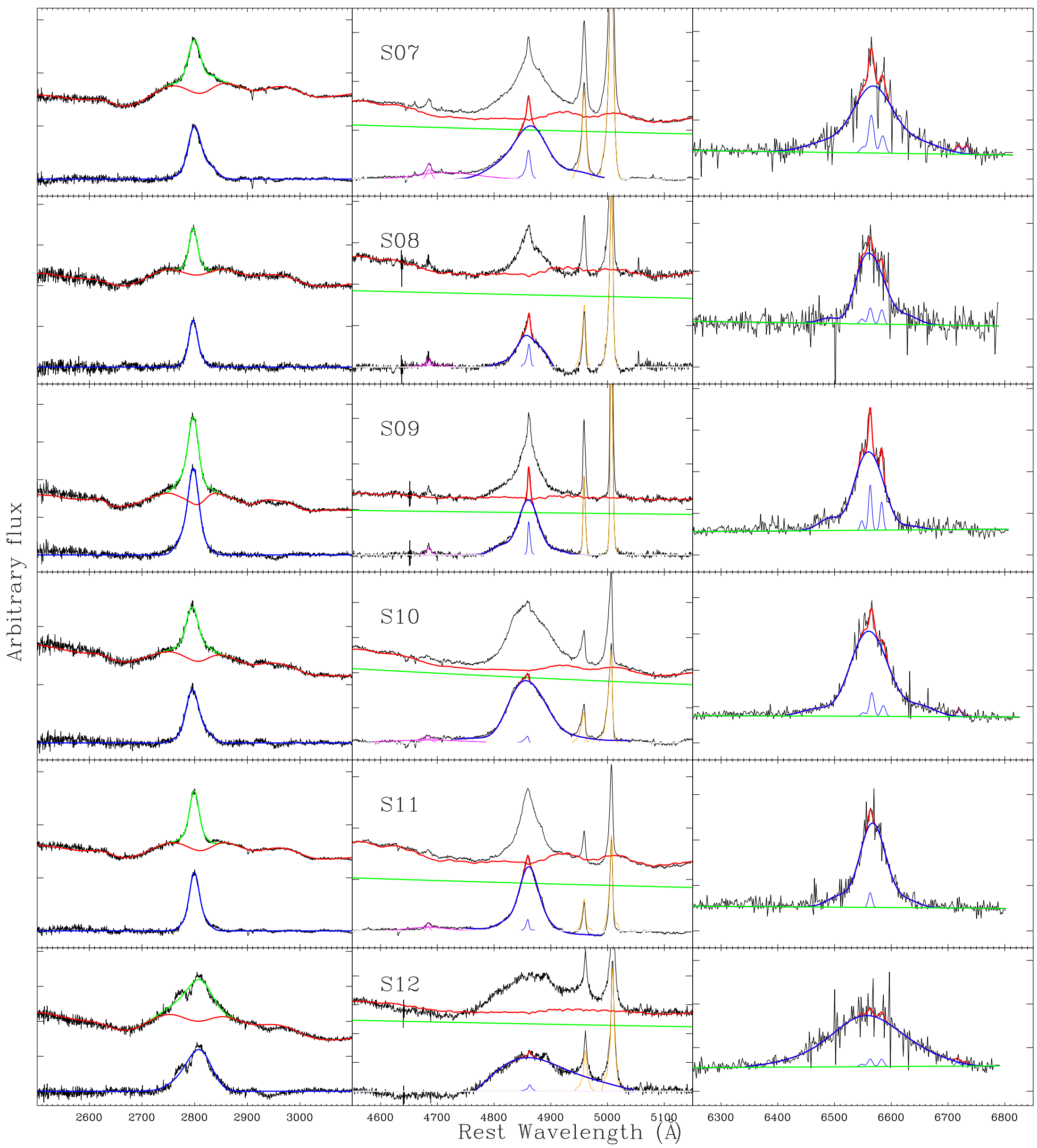

Figure 3.2: *Continued*

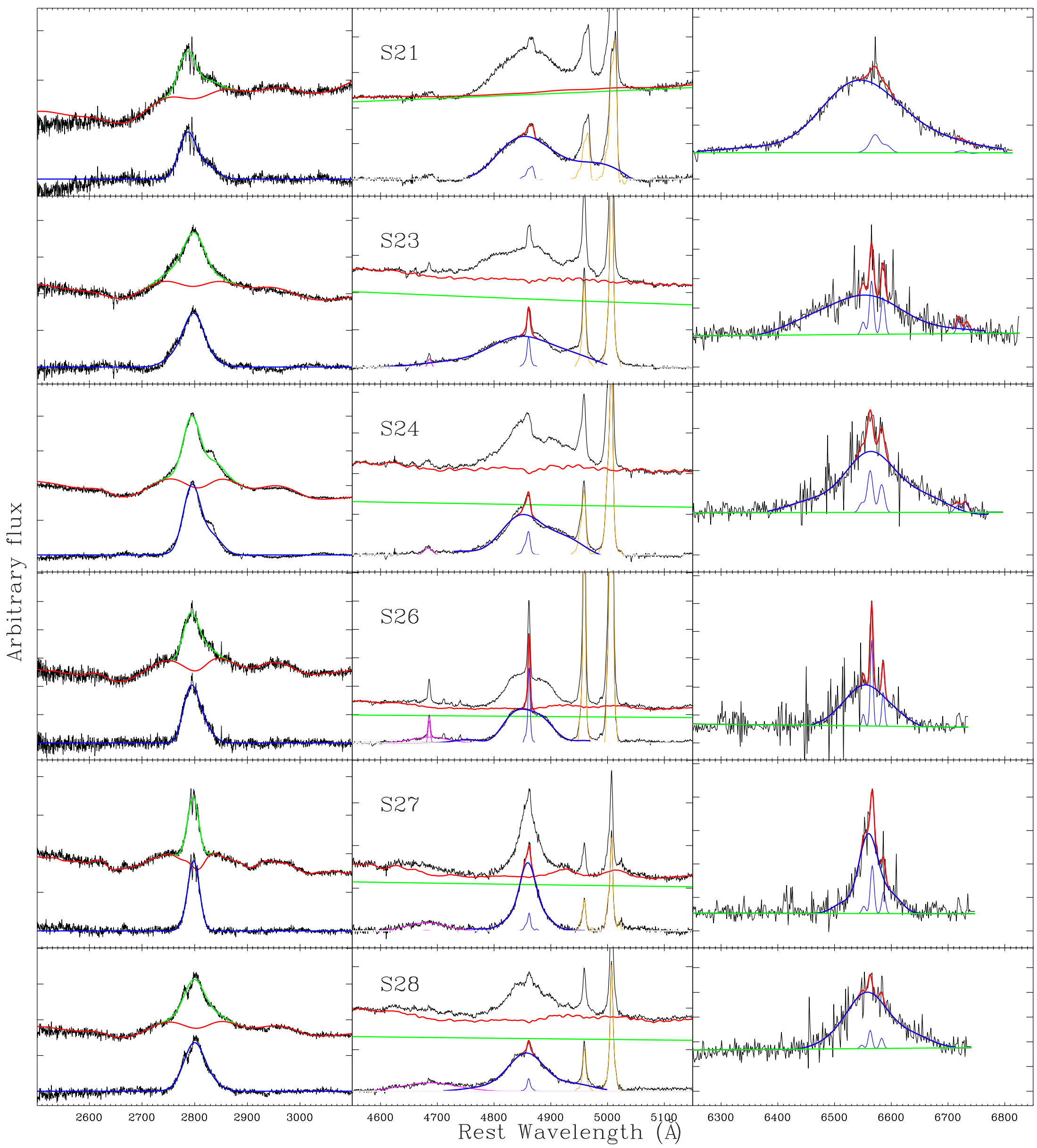

Figure 3.3: *Continued*

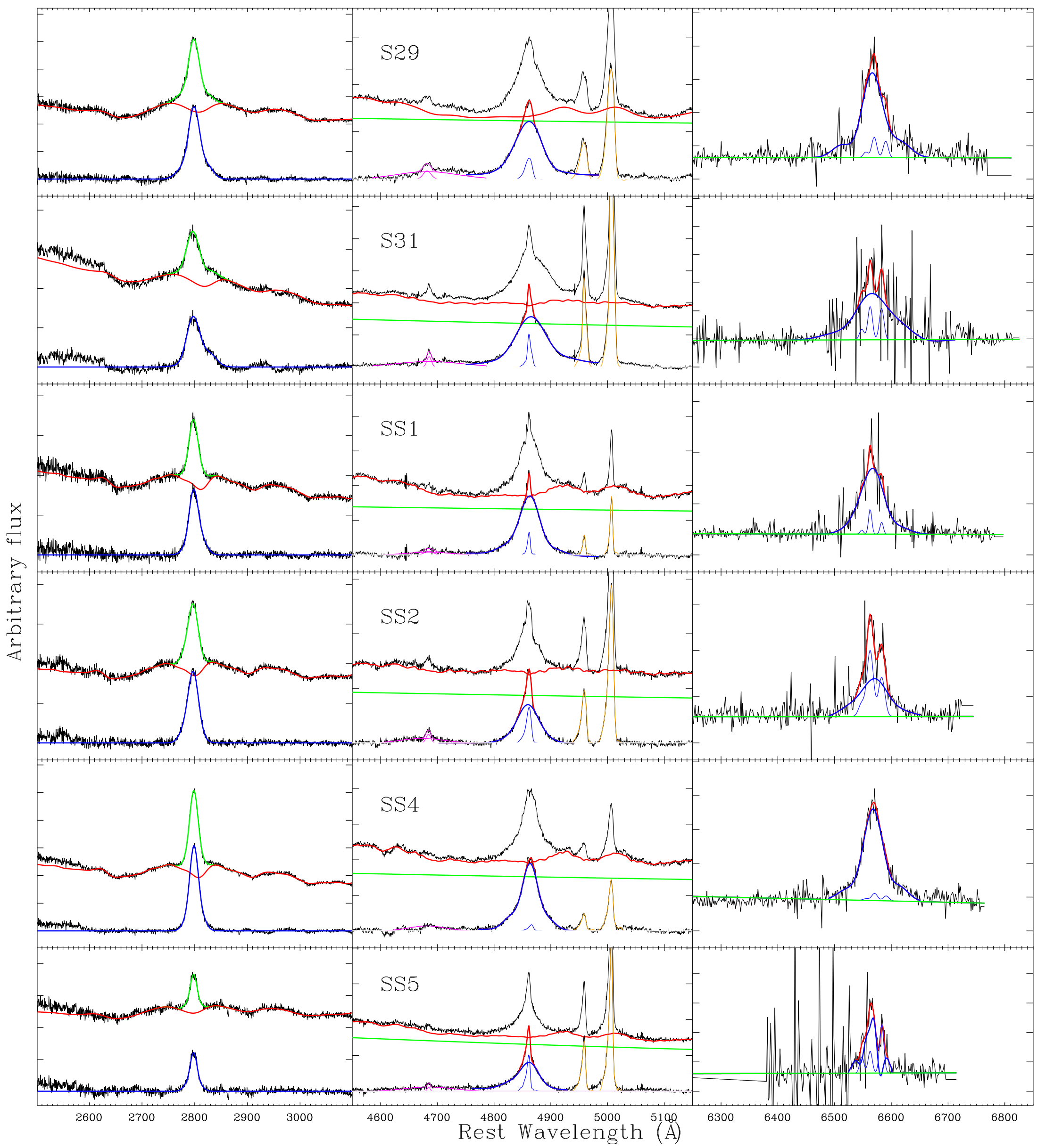

Figure 3.4: *Continued*

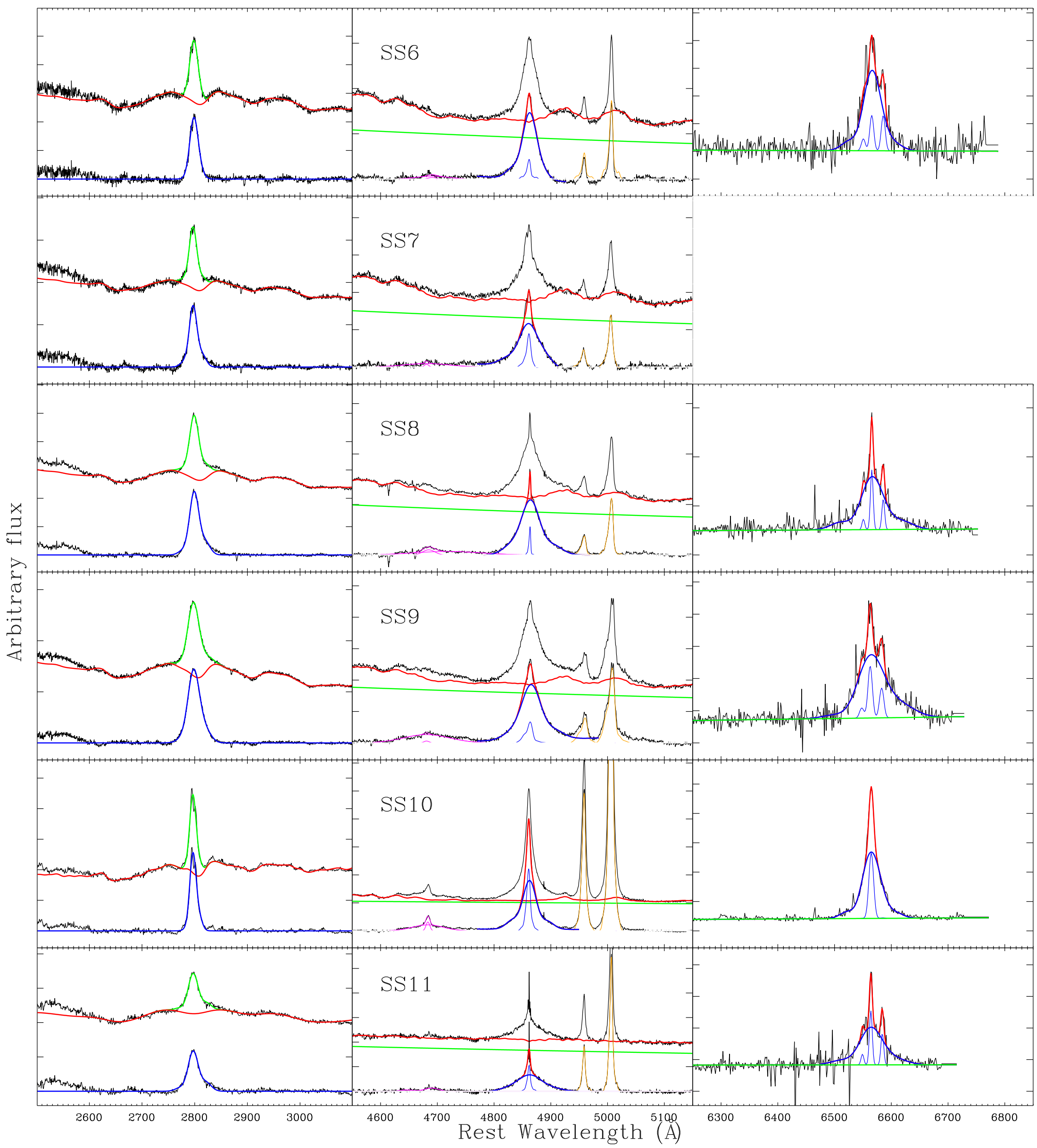

Figure 3.5: *Continued*

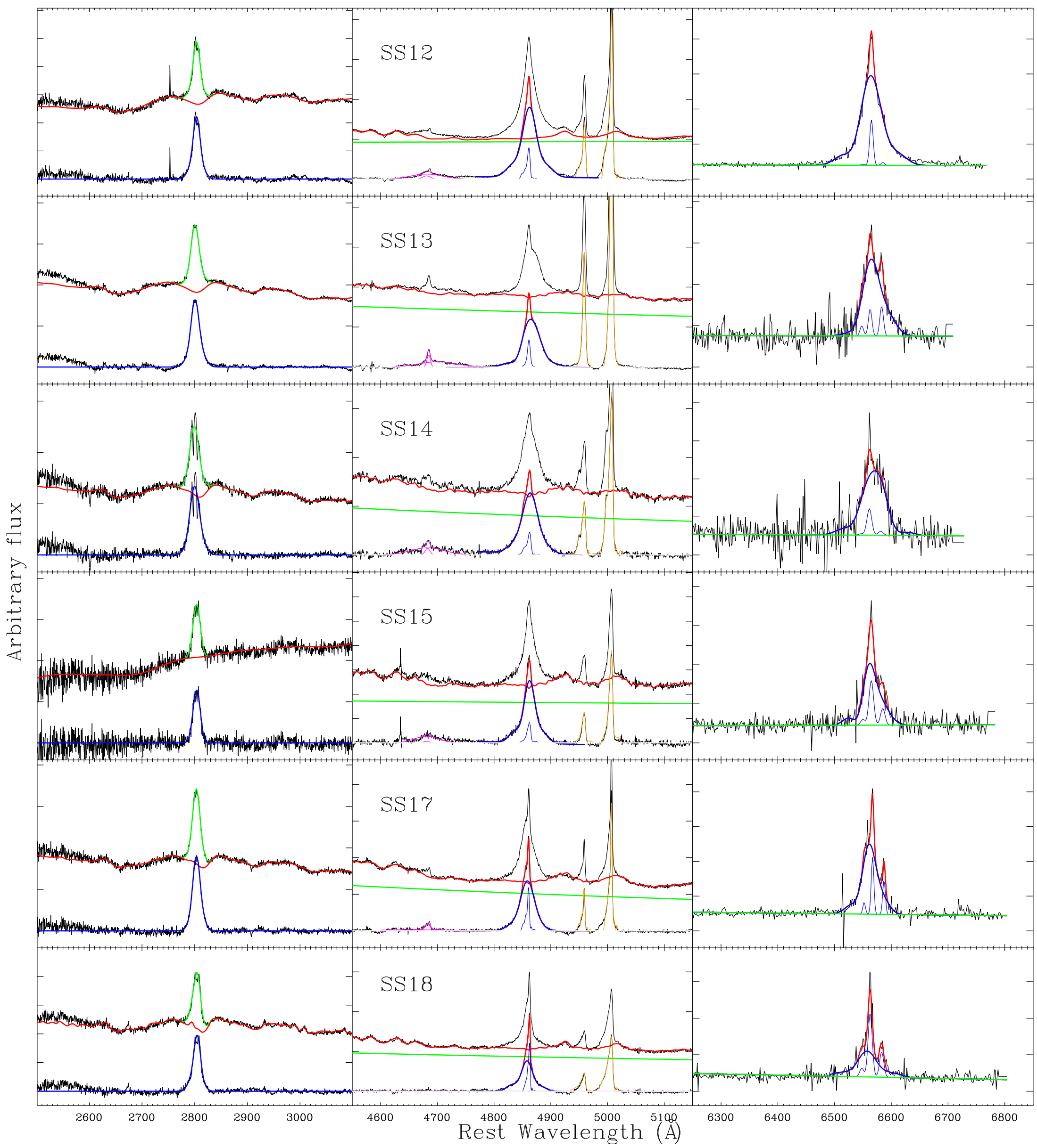

Figure 3.6: *Continued*

Table 3.1: Broad line widths & Continuum and line luminosities

Object	$FWHM_{H\alpha}$	$FWHM_{H\beta}$	$FWHM_{MgII}$	$\sigma_{H\alpha}$	$\sigma_{H\beta}$	σ_{MgII}	L_{3000}	L_{5100}	$L_{H\alpha}$	$L_{H\beta}$	L_{MgII}	$\frac{f(H\beta_{\rm NC})}{f([OIII]\lambda5007)}$
	(km s^{-1})			(km s^{-1})			(10^{44} erg s^{-1})		(10^{42} erg s^{-1})			
(1)	(2)	(3)	(4)	(5)	(6)	(7)	(8)	(9)	(10)	(11)	(12)	(13)
S01	4138	4489	3379	2570	2170	1888	2.15	1.55	5.96	1.85	3.52	0.13
S02	3723	4799	2919	2344	2197	1886	2.28	1.47	18.9	2.92	6.02	0.16
S03	2857	2984	2244	1938	1772	1259	4.92	2.74	11.7	3.56	4.50	0.21
S04	2632	2429	3064	1217	952	1570	2.28	1.99	4.03	0.66	3.63	0.08
S05	4316	4693	3883	3289	3390	2597	3.67	2.18	12.1	3.30	6.01	0.11
S06	3608	4708	3066	1387	1632	1478	3.46	1.82	2.34	1.07	3.66	0.11
S07	4129	4685	3409	2454	2631	1951	4.29	2.97	11.3	4.81	3.38	0.11
S08	2685	3268	2190	1526	1406	1091	2.48	2.45	4.13	0.90	1.07	0.12
S09	2746	2649	2886	1582	1672	1596	3.60	2.52	9.45	2.61	7.01	0.14
S10	3575	4763	3350	2106	2224	1805	7.02	3.67	16.1	5.15	6.38	0.07
S11	2529	2629	2596	1495	1434	1389	3.46	2.34	8.50	2.27	2.51	0.12
S12	7212	9331	6417	3254	3656	2853	5.13	2.87	13.4	3.66	7.92	0.05
S21	8013	7761	4701	4117	3874	2460	3.15	7.07	67.3	9.51	2.88	0.09
S23	8123	9868	5622	3492	4515	2752	3.81	2.94	13.1	3.78	5.64	0.11
S24	5667	7102	4683	2891	3046	2530	3.61	2.86	11.4	3.26	7.22	0.12
S26	4245	5416	4299	1685	2615	1884	2.48	1.78	7.68	3.17	2.83	0.08
S27	2039	2366	2846	1268	1330	1183	2.82	1.84	7.18	2.07	3.01	0.19

Col. (1): Target ID. Col. (2): FWHM of Hα line measured on the Gauss-Hermite model fit to SDSS data. Col. (3): FWHM of Hβ line measured on the Gauss-Hermite model fit to LRIS red data. Col. (4): FWHM of Mg II line measured on the Gauss-Hermite model fit to LRIS blue data. Col. (5): line dispersion of Hα line measured on the Gauss-Hermite model fit to SDSS data. Col. (6): line dispersion of Hβ line measured on the Gauss-Hermite model fit to LRIS red data. Col. (7): Line dispersion of Mg II line measured on the Gauss-Hermite model fit to LRIS blue data. Col. (8): Rest-frame luminosity at 3000 ÅĊol. (9): Rest-frame luminosity at 5100 Å . Col. (10): Rest-frame luminosity of Hα line. Col. (11): Rest-frame luminosity of Hβ line. Col. (12): Rest-frame luminosity of Mg II line. Col. (13): Ratio between $f(\mathrm{H}\beta_{\rm NC})$ and f([O III] λ5007).

Table 3.2: Broad line widths & Continuum and line luminosities

Object	$FWHM_{H\alpha}$ (km s^{-1})	$FWHM_{H\beta}$	$FWHM_{MgII}$	$\sigma_{H\alpha}$ (km s^{-1})	$\sigma_{H\beta}$	σ_{MgII}	L_{3000} (10^{44} erg s^{-1})	L_{5100}	$L_{H\alpha}$ (10^{42} erg s^{-1})	$L_{H\beta}$	L_{MgII}	$\frac{f(H\beta_{\rm NC})}{f([OIII]\lambda5007)}$
(1)	(2)	(3)	(4)	(5)	(6)	(7)	(8)	(9)	(10)	(11)	(12)	(13)
S28	4432	5051	5339	2174	3008	2427	2.64	2.35	6.60	2.47	3.91	0.10
S29	2018	3430	3000	1424	1644	1724	2.33	1.48	5.91	1.47	3.03	0.19
S31	3457	3913	3499	1624	2017	1964	3.66	2.84	9.15	3.11	3.59	0.12
SS1	2239	2693	2509	1173	1556	1224	2.64	2.04	6.50	2.05	2.49	0.39
SS2	2767	2827	2738	1352	1329	1226	1.80	1.84	3.20	1.01	1.77	0.23
SS4	1910	2207	2271	1191	1330	1069	1.84	1.83	5.42	1.56	2.43	0.12
SS5	−−	2619	1870	−−	1352	924	2.60	2.05	−−	1.02	0.87	0.24
SS6	1734	1958	2091	1003	1065	829	2.31	1.46	3.20	1.28	1.36	0.25
SS7	−−	2711	2030	−−	1217	1092	2.18	1.69	−−	1.04	1.39	0.64
SS8	2189	2593	2454	1448	1516	1340	3.30	2.29	5.56	2.32	2.69	0.50
SS9	2725	2684	3031	1535	1517	1475	3.37	2.24	6.98	2.21	4.27	0.28
SS10	1743	1797	1663	988	1198	695	5.21	4.23	20.1	5.20	3.79	0.15
SS11	2316	3486	2639	1328	1569	1578	3.75	2.96	4.31	1.24	2.14	0.19
SS12	1967	1888	1850	1202	1191	872	3.88	4.49	29.7	5.87	1.99	0.19
SS13	1802	2210	2183	913	1176	1042	2.78	2.06	4.18	1.17	1.98	0.08
SS14	2200	2082	2412	1114	1096	1073	1.84	1.09	2.99	0.89	1.82	0.14
SS15	1454	1486	1745	872	994	589	0.56	0.90	2.33	0.60	0.18	0.22
SS17	1431	1870	1925	815	963	825	3.74	2.21	5.57	1.66	2.93	0.34
SS18	1842	1510	1792	1171	1008	819	3.12	2.34	3.22	1.12	1.80	0.88

Table 3.1 Continued

3.1 The Hβ lines

Measuring the line width of Hβ requires careful fitting of the line profile and continuum since other emission features (e.g., Fe II , O III , and He II) are often blended with Hβ . For low luminosity AGN with relatively high host galaxy starlight, it is also necessary to subtract stellar absorption lines to precisely measure the line width of Hβ (Park et al. 2012). We adopt the multi-component spectral decomposition procedure described by Park et al. (2012), in order to separate the Hβ broad emission line from Fe II , O III , and He II , and stellar absorption lines. First, we fit the pseudo-continuum, which consists of a AGN power-law continuum, blended Fe II feature, and stellar absorption lines. Fe II feature was modelled by broadening the template provided from Boroson & Green (1992), which were convolved with various Gaussian velocities, while the stellar absorption lines were modelled by broadening a simple stellar population synthesis model of Bruzual & Charlot (2003) with solar metallicity and age of 11 Gyr. The stellar model component is essential for the accurate Hβ line width measurements since the stellar absorption line affects the center of the Hβ emission line, to which the FWHM of Hβ is very sensitive. The pseudo-continuum fitting is carried out in the regions of 4430Å - 4730Å and 5100Å - 5400Å, where Fe II feature is strong, using the non-linear Levenberg-Marquardt least-squares fitting routine `mpfit` in IDL (Markwardt 2009). The blue side window is slightly adjusted to avoid the Hβ or Hγ contamination if necessary. When the broad He II line is clearly separated from the Hβ profile, a double Gaussian model for the broad and narrow components of He II 4686Å line was simultaneously fitted with the pseudo-continuum. Then, we subtract the pseudo-continuum model from the observed rest-frame spectra.

After the pseudo-continuum subtraction, we model the [O III] 5007Å line with a tenth order Gauss-Hermite series to account for the significant blue wing of [O III] line profile, then use the same model for [O III] 4959Å by scaling the flux by 1/3. For Hβ, we fit the broad component with a sixth order Gauss-Hermite series while we used the

O III model for the narrow component of Hβ using a scale factor as listed in Table 3.1. When the Hβ line is blended with the He II line, He II broad and narrow components were fitted together with Hβ.

Based on these models, we measured the FWHM, line dispersion ($\sigma_{\mathrm{H}\beta}$), and luminosity of the Hβ broad component. L_{5100} was measured by averaging the flux between 5050Å $\sim$ 5150Å . Center columns of Figure 3.1 - 3.6 presents the observed Hβ region and the best-fit models for each component.

3.2 The Hα lines

Measuring the width of Hα is simpler than that of Hβ since Hα is stronger than Hβ and the Fe II feature is relatively weak in the Hα region. Since we are using relatively low quality SDSS spectra for fitting Hα, we do not attempt to fit the stellar absorption lines or Fe II feature. Instead, a featureless power-law can fit the observed continuum relatively well. Unfortunately, the Hα line is located at the red end of the SDSS spectral range due to the redshift of the sample. Thus, we model the continuum with a linear function using the rest frame 6100Å - 6300 Å region only. This region is relatively far from the blue wing of Hα, consequently not affected by the wings of Hα .

The Hα broad emission line is blended with the narrow Hα line, N II 6548Å, N II 6583Å, and also with two S II lines at 6716Å, 6731Å in broader Hα targets. Given the low quality of SDSS spectra, the detailed Gauss-Hermite series modelling of narrow line components did not improve the fitting result. Thus, we modelled all narrow emission lines as a single Gaussian component by fixing the width of narrow lines as same as the velocity of the narrow Hβ line, which is already determined from the Hβ region. In the χ^2 minimization process, all narrow line widths are fixed while their flux peaks are treated as free parameters with a constant flux ratio of 3 between two N II lines. We simultaneously fit all narrow lines and the broad Hα line using single Gaussian models and a Gauss-Hermite series, respectively. Then, we measure the FWHM, line

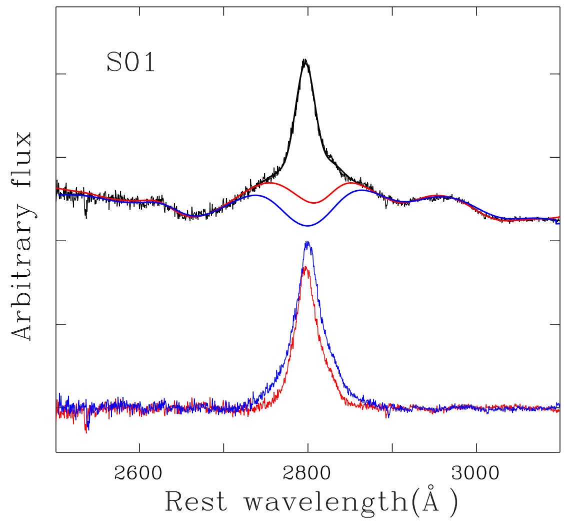

Figure 3.7: A comparison of Mg II line profiles when the Fe II emission blends are subtracted using the template from Vestergaard & Wilkes 2001 (*blue*) and Tsuzuki et al. 2006 (*red*), respectively.

dispersion, and luminosity of the broad Hα line from the best line profile model. Right columns of Figure 3.1 - 3.6 presents the observed Hα line and the best-fit model.

3.3 The Mg II lines

To measure the Mg II line widths, we first subtract power-law continuum and Fe II emission features by fitting the continuum window of 2600Å - 2750Å and 2850Å - 3090Å. Then, we fit the Mg II line with a sixth order Gauss-Hermite series. A narrow component of Mg II is not modelled because there is no significant feature implying the existence of narrow line.

On the other hand, we note that a careful treatment is required when dealing with Fe II emission in the region of Mg II line. The Fe II template provided by Vestergaard & Wilkes (2001) has been popularly used (e.g., Fine et al. (2008), Vestergaard & Osmer

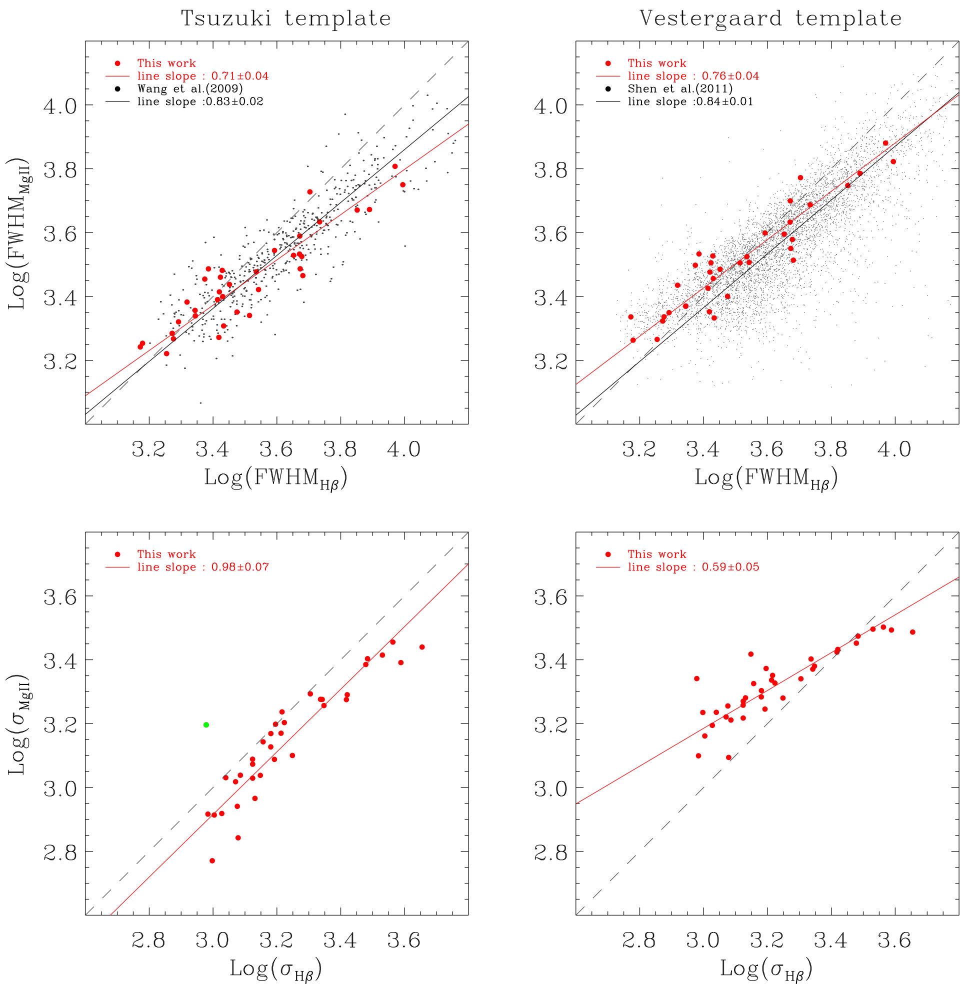

Figure 3.8: Measured Mg II line widths after Fe II and continuum subtraction using different templates. Slopes of regression line are marked as numbers in each panel *Upper left* : FWHM of Mg II and Hβ after the subtraction of Tsuzuki template. *Upper right* : FWHM of Mg II and Hβ after the subtraction of Vestergaard & Wilkes template. *Lower left* : Line dispersion (σ) of Mg II and Hβ after the subtraction of Tsuzuki template. *Lower right* : Line dispersion (σ) of Mg II and Hβ after the subtraction of Vestergaard & Wilkes template. Red dots are our measurements and small black dots are previous measurements by Wang et al. (2009) and Shen et al. (2011). Solid red lines are regression by OLS bisector method of our points, a green outlier (S04) in lower left panel was excluded in our line regression.

(2009), Shen et al. (2011)). However, the template contains no information of Fe II underneath the Mg II line because it was directly made from the observed spectrum of the narrow line Seyfert 1 galaxy, I Zwicky 1. In contrast, Tsuzuki et al. (2006) suggested another template based on the I Zwicky 1 template by adding the Fe II emission underneath the Mg II line, which were calculated with the one-dimensional photoionization model, CLOUDY(Ferland et al. 1998). Therefore, we investigate the difference of line width measurements using these two different templates (see also Wang et al. 2009). Figure 3.7 compares the best Fe II emission models using Vestergaard & Wilkes (2001) and Tsuzuki et al. (2006) templates, respectively for an object in our sample. The deblended Mg II line profile is narrower and weaker when using Tsuzuki et al. (2006) template than using Tsuzuki et al. (2006) template, since Fe II emission underneath of Mg II is removed.

To investigate which template is more appropriate, we compare the width of Hβ and the width of Mg II measured using two different templates. Upper two panels of Figure 3.8 compare FWHMs of Hβ and Mg II with different Fe II subtractions. Comparison between FWHMs of Mg II and Hβ shows non-linear proportionality and deviation from one-to-one relationship, indicating that the FWHMs of Mg II and Hβ are systematically different. To complement our comparison, we included available FWHM measurements from the literature. For example, Wang et al. (2009) investigated Mg II and Hβ FWHMs of 495 SDSS AGNs with $S/N \geq 20$ in both lines by measuring the $\mathrm{FWHM}_{\mathrm{MgII}}$ after subtracting Fe II based on Tsuzuki et al. (2006) template. In the case of Mg II measurements based on the template of Vestergaard & Wilkes (2001), we selected the sample of 4962 AGNs at $0.4 \leq z \leq 0.8$ with $S/N \geq 10$ in both emission lines from the catalog given in Shen et al. (2011) to ensure a rigorous comparison. Similar non-linear trend is present in the samples of Shen et al. (2011) and Wang et al. (2009), regardless of the template effect. As previous reported in Wang et al. (2009), these results imply that there is an intrinsic difference of the line profile or widths between

Hβ and Mg II although it is beyond the scope of the current work to investigate the origin of this difference. In practice, the non-linear proportionality indicates that it is necessary to introduce the different value of coefficient β in Eq. 3.1, in order to properly calibrate mass estimator based on $\mathrm{FWHM_{MgII}}$.

Lower two panels of Figure 3.8 compare the line dispersions of Mg II and Hβ. In these plots, we present our measurements only since line dispersion measurements are not available in the literature. The effect of Fe II template is clearly visible in the line dispersion comparison. When Tsuzuki template was used for measuring Mg II line dispersion, line dispersions of Mg II and Hβ show close linear relationship with a slight offset (bottom-left panel in Figure 3.8.) In contrast, there is a significant deviation from one-to-one relationship when Mg II line dispersion was measured using the Vestergaard & Wilkes template. This difference is interpreted as that the line dispersion of Mg II is overestimated compared to that of Hβ since Vestergaard & Wilkes template cannot properly subtract Fe II emission underlying the wings of the Mg II line as demonstrated in Figure 3.7. Therefore, we conclude that Tsuzuki temple provides more consistent line dispersion of Mg II compared to Hβ, and decided to use Tsuzuki template for subtracting Fe II in the Mg II region in the following analysis. FWHM, line dispersion and line luminosity were measured from Mg II model, while L_{3000} was measured from average flux between 2950Å $\sim$ 3050Å .

Chapter 4

Scaling Luminosities & line widths

Single-epoch M_{BH} can be described as a combination of two quantities is known, continuum luminosity and broad line width, as expressed in Eq. 3.1. We adopted the estimator based on $\sigma_{H\beta}$ and continuum luminosity at 5100Å combined with the virial assumption and the size-luminosity relation from Bentz et al. (2006) as our fiducial M_{BH} (Bennert et al. 2010). As a first step, for establishing new M_{BH} equations for the other combinations, we investigate scaling relations among luminosities and line width, to decide β and γ in Eq. 3.1.

4.1 Line widths

As described in Section 3.3, scaling the line widths is very important to properly calibrate the Mg II line width since it shows the systematic difference with that of Hβ line. For FWHM, Mg II and Hβ line widths show the difference with a non-unity slope as found in many previous studies (e.g., Salviander et al. (2007), Wang et al. (2009), and Shen et al. (2011)). Upper two panels of Figure 3.8 contain a direct comparison between FWHMs of Mg II and Hβ and indicate that this trend is not stemming from the choice of template for Fe II emission. We find slightly shallower slopes than the previous results from Wang et al. (2009) and Shen et al. (2011), since they modelled the Mg II line profile with a narrow component.

In the case of line dispersions, we could not compare our results with the previous measurements since they did not measure the line dispersion due to the low quality of spectra. Lower two panels of Figure 3.8 show a comparison between Mg II and Hβ line dispersions of this work and show a clear dependency on the template used for the Fe II subtraction. As described in Section 3.3, the subtraction using the template from Vestergaard & Wilkes (2001) produces unbelievable line dispersion measurements due to the its lack of Fe II near 2800 Å region, while the measured Mg II line dispersion using Tsuzuki et al. (2006) template shows almost one-to-one relationship with Hβ line dispersion with slight systematic offset of ~ 0.09 dex. In this comparison, we exclude one outlier, S04, because of its Hβ profile shows very wide flat feature under the Hβ even after the proper stellar and Fe II subtraction, then the measurement of Hβ could be underestimated.

Finally, we determine β, which properly scales the Mg II line width to the Hβ line widths, with the following relations,

$$\log(FWHM_{MgII}) \propto 0.71 \pm 0.04 \times \log(FWHM_{H\beta}) \tag{4.1}$$

$$\log(\sigma_{MgII}) \propto 0.98 \pm 0.08 \times \log(\sigma_{H\beta}). \tag{4.2}$$

Therefore our recipes using Mg II line width will contain ${FWHM_{MgII}}^{2/0.71}$ or ${\sigma_{MgII}}^{2/0.98}$ as the M_{BH} estimator.

For Balmer lines, we simply adopt a result of Greene & Ho (2005), who concluded a simple one-to-one relationship between Hα and Hβ FWHMs. Their conclusion is physically reasonable since Hα and Hβ emitting sources are intrinsically same. We use

$\beta\ = 2$ in Equation 3.1 for both FWHM and $\sigma_{\rm line}$ as our $M_{\rm BH}$ estimator.

4.2 Luminosities

Based on previous reverberation mapping studies (i.e., McLure & Jarvis 2002; Kaspi et al. 2005; Bentz et al. 2009), an empirical relation was derived for substituting a BLR size with AGN luminosities. Series of studies suggested a possibility of Balmer line luminosity instead of continuum luminosity a proxy for the BLR size $M_{\rm BH}$ estimators (e.g., Greene & Ho 2005, Vestergaard & Peterson 2006). McGill et al. (2008) adopted this concept with the Mg II line luminosity. We tried to verify the reliability of line luminosities for $M_{\rm BH}$ estimators using our enlarged sample.

In this section, we compared several continuum and line luminosities with the best studied L_{5100} in our data set, then extended the size-luminosity relation to other luminosities based on this comparison. Our comparisons of all measured luminosities are plotted in Figure 4.1. Prior to calculating the slope, we excluded two objects, S21 and SS15, from the $L_{5100} - L_{3000}$ comparison plot since they showed high internal extinction spectra.

However, this direct luminosity comparison contains an intrinsic problem due to the high stellar light contamination. Since stellar light contamination is not negligible, L_{5100} of low luminosity AGNs are relatively higher than other luminosities , i.e., L_{3000} and line luminosities in Figure 4.1, leading to a steep regression slope. Similar phenomenon is also found in the measurements of Shen et al. (2011) which were based on SDSS data. This result implies that our measured L_{5100} contains contribution from stellar luminosities since our target AGNs have relatively higher stellar light fraction in the observed spectra. Unfortunately, this contamination still remains when we use AGN power-law luminosity to measure AGN continuum luminosity after removing stellar lights (L_{5100de}) based on our spectral decomposition. Figure 4.2 compares luminosities between L_{5100de} and other luminosities, and upper two panels shows the remaining

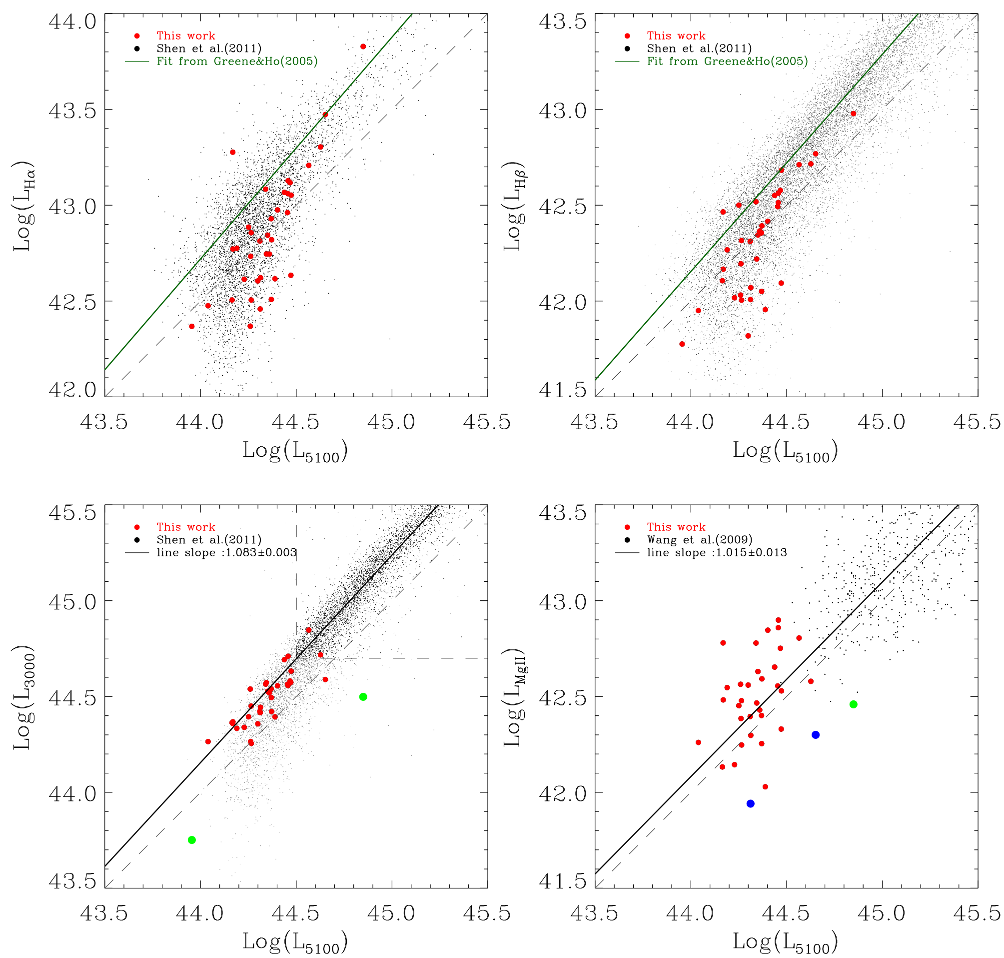

Figure 4.1: Correlations between L_{5100} and other luminosities. X axises are the continuum luminosity at 5100 Å obtained from spectral decomposition of LRIS red CCD spectra, while y axises are continuum luminosity at 3000 Å and broad emission line luminosities. In lower left panel, black dots are 495 targets of Wang et al. (2009), specially selected from SDSS catalog. In other cases, dots are data from SDSS catalog of Shen et al. (2011), with S/N ratio grater than 10, but the target pool is different in each panel due to the spectral range of SDSS. Solid green lines in upper panels show the relation of Greene & Ho (2005), while solid red and black lines are regression lines of our targets and SDSS catalog obtained by OLS bisector regression analysis. Note that two green outliers, S21 and SS15, which show heavy internal extinction in Figure 2.1 and 2.2, are excluded from our line regression in upper left and lower right panel, but two blue points, SS5 and SS12, are still included. Black dashed box in lower left panel means our arbitrary high luminosity cut for SDSS data.

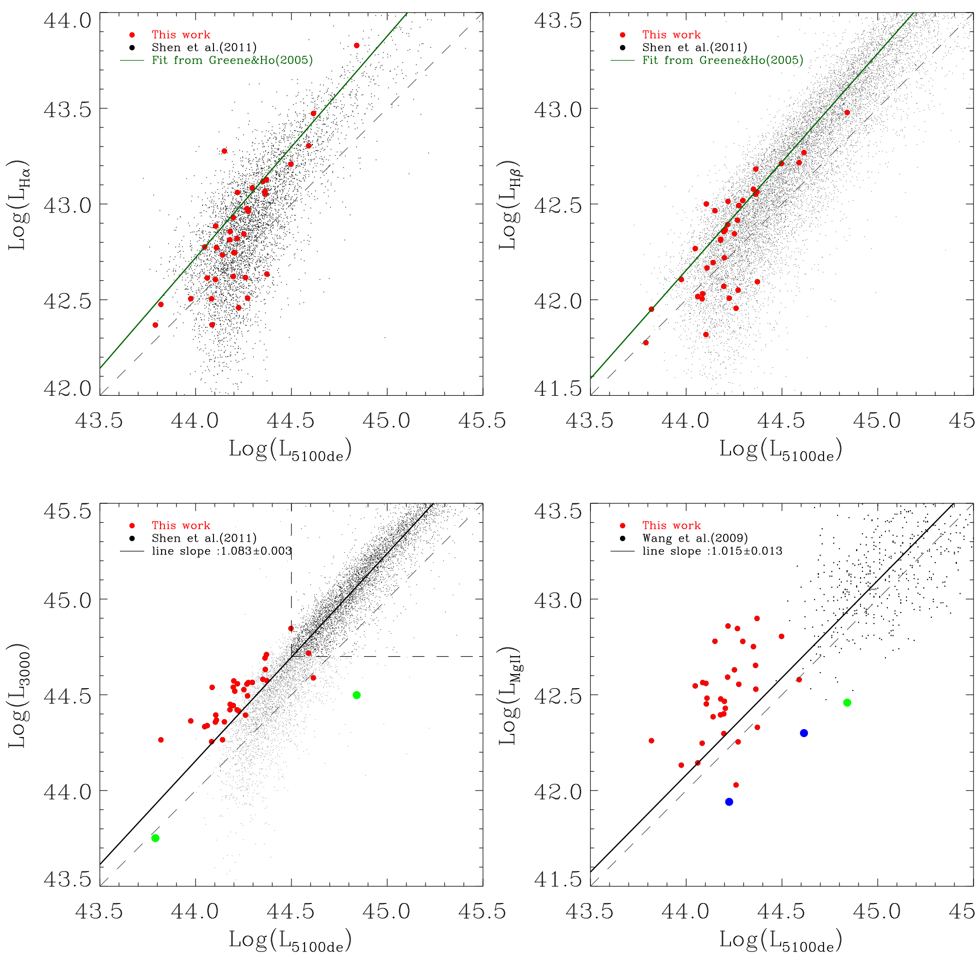

Figure 4.2: Similar with Fig 4.1, but using L_{5100} measured from the power-law continuum after subtracting Fe II and stellar component

contamination.

To solve this problem and scale luminosity as a BLR size, we need to check previous results. First, for scaling Balmer line luminosities, we used the result of Greene & Ho (2005) who selected a AGN sample with negligible host-galaxy contamination. In Figure 2 of that paper, a comparison between L_{5100} and $L_{H\alpha}$ showed a slope of 1.157, while a slope of L_{5100} versus $L_{H\beta}$ was 1.133. In upper two panel of Figure 4.1, equations from Greene & Ho (2005) are denoted as green lines, showing consistency with the high-luminosity SDSS AGNs from Shen et al. (2011), for which stellar light contamination is also negligible. Thus, we decided to use the slopes from Greene & Ho (2005) for the Balmer line luminosity scaling, leading to M_{BH} estimators as following relations.

$$\log(L_{H\alpha}) \propto 1.157 \times \log(L_{5100}) \tag{4.3}$$

$$\log(L_{H\beta}) \propto 1.133 \times \log(L_{5100}). \tag{4.4}$$

For L_{3000} and L_{5100}, we adopt an arbitrary high luminosity cut and extrapolate a regression result of higher luminosity points of SDSS catalog. In this case, the extrapolated regression is very close to one-to-one relation with small offset, and also shows consistency with our data points. Therefore estimator of L_{5100} also can be adopted for L_{3000}. Also this consistency with L_{5100} and L_{3000} suggests a possibility of stellar light contamination in 3000 Å from young blue stars, which can be inferred by the fact that seven of our targets show star formation rate by 3.3 μm polycyclic aromatic hydrocarbon emission (Woo et al. 2012).

Finally, for the L_{MgII} in lower right panel in Figure 4.1, measurements are taken from Wang et al. (2009) since they used the same Fe II template for measuring the Mg II line width and luminosity. Similar to the L_{3000} case, regression based on Wang et al. (2009) shows a slope almost one, then it is reasonable to conclude that L_{MgII} and L_{5100} have similar relation with BLR size.

Based on comparison that we have presented in this section, we determine γ for each luminosity: 0.448 for Hα , 0.457 for Hβ using Equation 4.3 and 4.4, and 0.518 for L_{3000} and $L_{\rm MgII}$ because regressions between L_{5100} and these luminosities are almost 1.

slopes in Figure 4.1 are almost 1.

Chapter 5

Calibrating M_{BH} estimators

In this section, we finally calibrate the normalization constant α in Equation 3.1, for each line width and luminosity combination, and determine M_{BH} estimators. We fix the values β and γ obtained from Section 4.1 and 4.2 and then determine α by fitting M_{BH} estimates from each estimator with the best M_{BH} using χ^2 minimization method. As noted in Section 4, we use the M_{BH} estimated with $\sigma_{H\beta}$ and L_{5100} as the best M_{BH} because the Hβ line is the best-calibrated broad emission line based on the reverberation mapping data. Newly determined M_{BH} with the determined α are shown in Figure 5.1 and 5.2.

5.1 M_{BH} recipes for Balmer lines

In Figure 5.1, we plotted our calibrations for Hα and Hβ emission lines. The value of α is estimated from this comparison fit while the β is fixed to be 2 and the γ has the value from Section 4. Note that the rms scatter, which is given in the lower-right corner of each panel, reflects uncertainty of the newly derived mass estimators Although L_{5100} shows the best agreement, $L_{H\alpha}$ and $L_{H\beta}$ give relatively good agreement with a scatter of < 0.16 dex. For the velocity estimator, line dispersion ($\sigma_{\rm line}$) usually shows less scatter than FWHM, but the difference between $\sigma_{\rm line}$ and FWHM is not remarkable

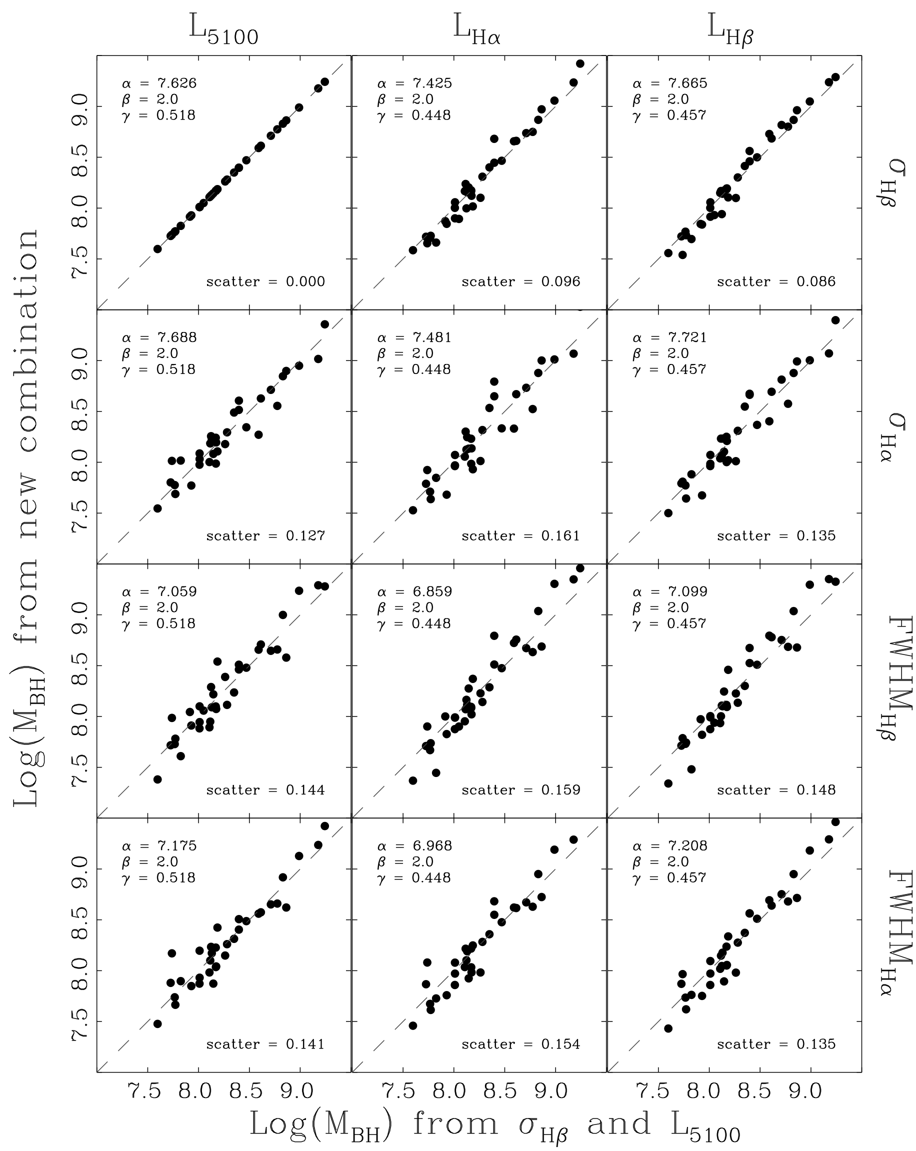

Figure 5.1: Cross-calibration fitting between newly derived $M_{\rm BH}$ and fiducial mass with estimators from Balmer lines. X axis data points represent our target's fiducial mass, while y axis data points are $M_{\rm BH}$ from $\alpha + \beta \log v_{1000} + \gamma \log L$. v_{1000} means velocity estimator using 1000 $km\ s^{-1}$ unit, L is luminosity estimator having 10^{44} $erg\ s^{-1}$ unit for continuum or 10^{42} $erg\ s^{-1}$ unit for emission line. β and γ in each panel depend on a kind of estimators which are shown in upper and left part of figure, and α is estimated by χ^2 minimization fitting.

except for Hβ .

By comparing our result with the Table 3 of McGill et al. (2008), we find an improvement of our result. In addition to enlarging the sample size and dynamical range, scatters of newly derived $\rm M_{BH}$ are reduced by $0.05 - 0.15$ dex compared to McGill's result and the signs of systematic uncertainty also disappeared.

5.2 $\rm M_{BH}$ recipes for Mg II line

We compared $\rm M_{BH}$ from Mg II lines with that from Hβ in this section. Differing from the calibration of Balmer lines, we used the scaled value for the β derived from Section 4 but not γ because there are not negligible difference between the line widths from Mg II and Hβ . A result of calibrating Mg II estimators is shown in Figure 5.2. Although Mg II based $\rm M_{BH}$ s show more scatter than the those of the Balmer lines, each combination shows good correlation with the fiducial $\rm M_{BH}$ with the scatter of < 0.27 dex, suggesting more reliable $\rm M_{BH}$ s compared with the recipes from McGill et al. (2009) with $0.03 \sim 0.05$ dex less scatter. This also shows possibility of using Mg II line luminosity as a BLR size indicator in an $\rm M_{BH}$ estimators.

In addition,we find another interesting fact about $\rm M_{BH}$ based on Mg II . Regarding the uncertainty of FWHM - based $\rm M_{BH}$ and σ_{MgII} based $\rm M_{BH}$, the latter is consistent with the fiducial $\rm M_{BH}$ with ~ 0.4 dex scatter although the difference is not significant in case of Hα, which is probably due to the lower quality SDSS spectra. Considering the quality of our spectra, we suggest that a reliability of $\rm M_{BH}$ will be $\sim 15\%$ improved when using σ, especially for high S/N spectra.

By comparing with previous studies of the Mg II line, we obtained better agreement with ~ 0.5 dex larger mass range and twice larger sample compared with McGill et al. (2008). The luminosity range of our samples is ~ 0.7 dex lower than that of Wang et al. (2009), providing $\rm M_{BH}$ recipes for low luminosity AGNs.

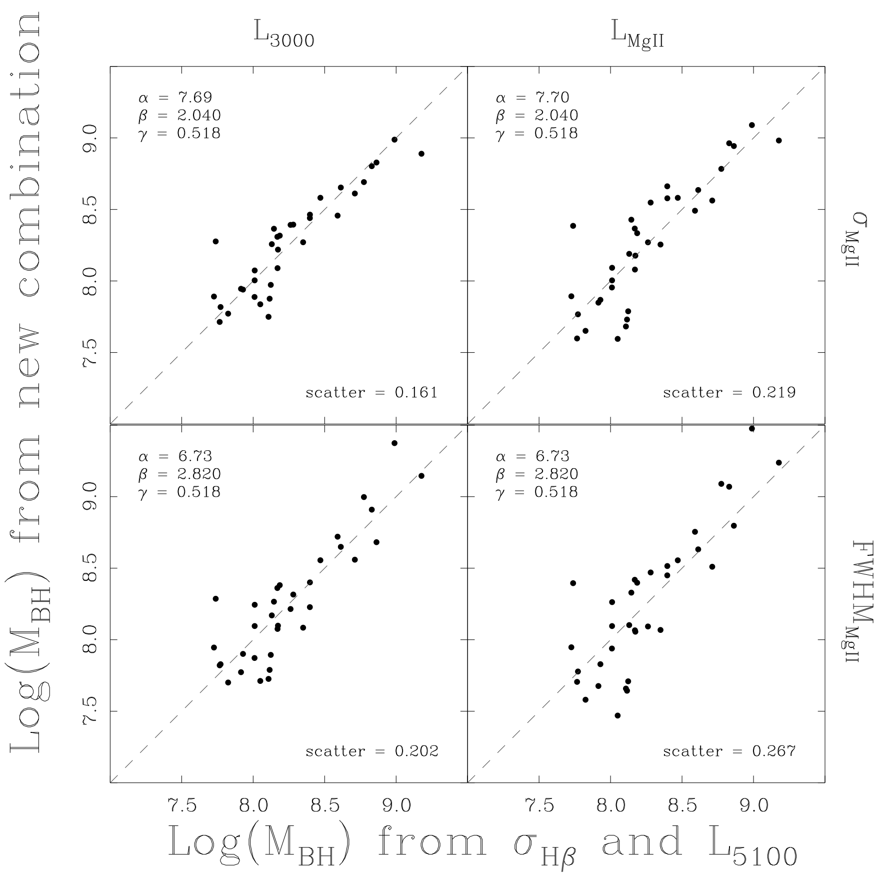

Figure 5.2: Cross-calibration fitting between the newly induced $\rm M_{BH}$ and fiducial mass with estimators from Mg II lines. The equation of $\rm M_{BH}$ can be represented as a combination of estimators and α,β and γ. It is noticing that S21 and SS15 are not included in this analysis.

Chapter 6

Summary

In this paper, we have presented a calibration of M_{BH} estimators using Keck and SDSS spectra of 35 AGNs at z=0.36 with BH masses of $10^{7.5-9}M_{\odot}$. Our results are summarized as follows:

(1) In Section 3, we analyzed three major broad emission lines, Hα, Hβ, and Mg II with a multi-component spectral analysis method. AGN power-law continuum, Fe II emissions, and stellar spectra are removed if necessary, then the pure broad emission line was fitted with the Gauss-Hermite series. We measured FWHM, line dispersion, and luminosity of each broad emission line. There is found a systematic difference of Mg II line widths depending on the choice of Fe II templates applied.

(2) By comparing the line width and luminosity measurements from our data and previous works, we determined scaling coefficient of each luminosity and velocity estimators in Section 4, i.e, $FWHM_{H\beta} \propto FWHM_{MgII}{}^{1.408}$, $\sigma_{H\beta} \propto \sigma_{MgII}{}^{1.020}$ and $L_{5100} \propto L_{H\alpha}{}^{0.864}$, $L_{H\beta}{}^{0.883}$.

(3) We performed a cross-calibration of newly derived equations in Section 5, based on various combinations of velocity and luminosity indicators measured from Hα Hβ and Mg II lines. Setting M_{BH} estimated with $\sigma_{H\beta}$ and L_{5100} as our fiducial mass, we determined an uncertainty of each estimator by quantifying a scatter of new M_{BH}

estimates compared to the fiducial M_{BH} estimates. All combinations using Balmer lines provide reliable equation with a scatter less than 0.16 dex. Especially the combinations of the continuum luminosity and line dispersion show the best reliability. For Mg II, a combination of L_{3000} and σ_{MgII} gives the best reliability with 0.16 dex scatter, but other combination with $FWHM_{\rm MgII}$ or $L_{\rm MgII}$ are more uncertain with scatter ~ 0.27 dex. Our result suggests that M_{BH} based on σ_{line} is more reliable than that based on FWHM, especially with good quality spectra. These new single - epoch M_{BH} estimators will be useful to study AGN in broad range of luminosity and mass.

Bibliography

Assef, R. J., Denney, K. D., Kochanek, C. S., et al. 2011, ApJ, 742, 93

Barth, A. J., Pancoast, A., Thorman, S. J., et al. 2011, ApJ, 743, L4

Bennert, V. N., Treu, T., Woo, J.-H., et al. 2010, ApJ, 708, 1507

Bennert, V. N., Auger, M. W., Treu, T., Woo, J.-H., & Malkan, M. A. 2011, ApJ, 742, 107

Bentz, M. C., Peterson, B. M., Pogge, R. W., Vestergaard, M., & Onken, C. A. 2006, ApJ, 644, 133

Bentz, M. C., Peterson, B. M., Netzer, H., Pogge, R. W., & Vestergaard, M. 2009, ApJ, 697, 160

Blandford, R. D., & McKee, C. F. 1982, ApJ, 255, 419

Boroson, T. A., & Green, R. F. 1992, ApJS, 80, 109

Bruhweiler, F., & Verner, E. 2008, ApJ, 675, 83

Bruzual, G., & Charlot, S. 2003, MNRAS, 344, 1000

Denney, K. D., Peterson, B. M., Pogge, R. W., et al. 2010, ApJ, 721, 715

Ferland, G. J., Korista, K. T., Verner, D. A., et al. 1998, PASP, 110, 761

Ferrarese, L., & Merritt, D. 2000, ApJ, 539, L9

Ferrarese, L., & Ford, H. 2005, Space Sci. Rev., 116, 523

Fine, S., Croom, S. M., Hopkins, P. F., et al. 2008, MNRAS, 390, 1413

Gebhardt, K., Bender, R., Bower, G., et al. 2000, ApJ, 539, L13

Greene, J. E., & Ho, L. C. 2005, ApJ, 630, 122

Grier, C. J., Peterson, B. M., Pogge, R. W., et al. 2012, arXiv:1206.6523

Gültekin, K., Richstone, D. O., Gebhardt, K., et al. 2009, ApJ, 698, 198

Kaspi, S., Smith, P. S., Netzer, H., et al. 2000, ApJ, 533, 631

Kaspi, S., Maoz, D., Netzer, H., et al. 2005, ApJ, 629, 61

Kim, D., Im, M., & Kim, M. 2010, ApJ, 724, 386

Kormendy, J., & Richstone, D. 1995, ARA&A, 33, 581

Markwardt, C. B. 2009, in Astronomical Data Analysis Software and Systems XVIII, ed. D. A. Bohlender, D. Durand, & P. Dowler (San Francisco: ASP), 251

McGill, K. L., Woo, J.-H., Treu, T., & Malkan, M. A. 2008, ApJ, 673, 703

McLure, R. J., & Dunlop, J. S. 2002, MNRAS, 331, 795

McLure, R. J., & Dunlop, J. S. 2004, MNRAS, 352, 1390

McLure, R. J., & Jarvis, M. J. 2002, MNRAS, 337, 109

Onken, C. A., Ferrarese, L., Merritt, D., et al. 2004, ApJ, 615, 645

Park, D., Woo, J.-H., Treu, T., et al. 2012, ApJ, 747, 30

Peterson, B. M. 1993, PASP, 105, 247

Peterson, B. M., Ferrarese, L., Gilbert, K. M., et al. 2004, ApJ, 613, 682

Salviander, S., Shields, G. A., Gebhardt, K., & Bonning, E. W. 2007, ApJ, 662, 131

Schlegel, D. J., Finkbeiner, D. P., & Davis, M. 1998, ApJ, 500, 525

Shen, Y., Richards, G. T., Strauss, M. A., et al. 2011, ApJS, 194, 45

Shen, Y., & Liu, X. 2012, ApJ, 753, 125

Treu, T., Malkan, M. A., & Blandford, R. D. 2004, ApJ, 615, L97

Treu, T., Woo, J.-H., Malkan, M. A., & Blandford, R. D. 2007, ApJ, 667, 117

Tsuzuki, Y., Kawara, K., Yoshii, Y., et al. 2006, ApJ, 650, 57

Vanden Berk, D. E., Richards, G. T., Bauer, A., et al. 2001, AJ, 122, 549

van Dokkum, P. G. 2001, PASP, 113, 1420

Vestergaard, M. 2004, ApJ, 601, 676

Vestergaard, M., & Osmer, P. S. 2009, ApJ, 699, 800

Vestergaard, M., & Peterson, B. M. 2006, ApJ, 641, 689

Vestergaard, M., & Wilkes, B. J. 2001, ApJS, 134, 1

Wandel, A., Peterson, B. M., & Malkan, M. A. 1999, ApJ, 526, 579

Wang, J.-G., Dong, X.-B., Wang, T.-G., et al. 2009, ApJ, 707, 1334

Wills, B. J., Netzer, H., & Wills, D. 1985, ApJ, 288, 94

Woo, J.-H., Treu, T., Malkan, M. A., & Blandford, R. D. 2006, ApJ, 645, 900

Woo, J.-H. 2008, AJ, 135, 1849

Woo, J.-H., Treu, T., Barth, A. J., et al. 2010, ApJ, 716, 269

Woo, J.-H., Kim, J. H., Imanishi, M., & Park, D. 2012, AJ, 143, 49

Woo, J.-H., & Urry, M., 2002, ApJ, 579, 530

요 약

21세기 들어 대부분의 은하의 중심에 거대 블랙홀이 위치한다는 사실이 널리 받아들여 지고 있다. 이런 블랙홀들은 단지 존재할 뿐 아니라 모 은하와 다양한 상관 관계를 보임으로 인해 모 은하의 진화에도 밀접하게 연관되어 있으리라 여겨지고, 따라서 거대 블랙홀을 연구하는 것은 은하 자체를 연구하는 데에 있어서도 중요한 부분이다.

많은 선행 연구를 통해, 블랙홀의 질량은 활동성 은하핵의 경우 넓은 방출선의 선폭과 연속선 또는 방출선의 광도의 조합으로 나타낼 수 있다는 사실이 알려지게 되었다. 이 연구에서는 적색 편이 0.4정도에 위치하는 36개의 타입 1 활동성 은하핵을 분광 관측하여 그 중심에 있는 거대 블랙홀의 질량을 추산하는 여러 방법들을 비교 분석하였다. 켁 망원경으로 관측하여 신호 대 잡음 비가 100을 넘어서는 좋은 관측 자료와, 공개된 자료인 슬로안 디지털 하늘 탐사(Sloan Digital Sky Survey, SDSS) 에서 얻은 자료를 합하여 우리는 활동성 은하핵의 주요한 넓은 방출선들인 Hα 6563 Å, Hβ 4861 Å , 그리고 Mg II 2800 Å 의 세 방출선을 모든 대상에 대해 얻을 수 있었다.

가장 믿을 만한 블랙홀 질량을 제공한다고 여겨지는 Hβ 의 속도 분산과 5100 Å 의 연속선 광도로 구성되는 블랙홀 질량을 기준으로 하여 우리는 측정한 여러 방출선들의 선폭(Full-width at half maximum, FWHM) 과 속도 분산, 연속선 광도와 방출선 광도를 여러 가지 방식으로 조합하여 다양한 블랙홀 질량 공식을 이끌어 내었으며, 시험해 본 모든 조합의 블랙홀 질량 공식이 기준이 되는 질량과 비교하였다. 발머 계열 방출선을 이용한 블랙홀 질량들은 기준 질량과 비교하여 로그 단위에서 0.2 미만의 데이터 분산을 보였고, 마그네슘 라인을 이용한 블랙홀 질량 공식은 발머 계열의 신뢰도보다 다소 떨어지긴 하지만 로그 단위로 0.27 미만의 데이터 분산을 보임으로써 우리가 새로 이끌어낸 블랙홀 질량들이 신뢰할 만함을 입증하였다.

주요어:블랙홀 — 은하: 활동성 은하핵 — 은하: 진화 — 퀘이사

학 번: 2010 – 20389